Water Research 188 (2021) 116536

Contents lists available at ScienceDirect

Water Research

journal homepage: www.elsevier.com/locate/watres

Modeling the impact of evolving biofilms on flow in porous media inside a microfluidic channel

Shahab Karimifard[a], Xu Li[a], Christian Elowsky[b], Yusong Li[a,*]

[a] Department of Civil and Environmental Engineering, University of Nebraska-Lincoln, Lincoln, NE, 68588, United States
[b] Department of Agronomy and Horticulture, University of Nebraska-Lincoln, Lincoln, NE 68583, United States

ARTICLE INFO

Article history:
Received 3 June 2020
Revised 22 September 2020
Accepted 18 October 2020
Available online 19 October 2020

Keywords:
Biofilms
Hydrodynamics
Microfluidics
Permeability
Porous media

ABSTRACT

This study integrates microfluidic experiments and mathematical modeling to study the impacts of biofilms on flow in porous media and to explore approaches to simplify modeling permeability with complicated biofilm geometries. *E. coli* biofilms were grown in a microfluidic channel packed with a single layer of glass beads to reach three biofilm levels: low, intermediate, and high, with biofilm ratios (β_r) of 2.7%, 17.6%, and 55.2%, respectively. Two-dimensional biofilm structures and distributions in the porous medium were modeled by digitizing confocal images and considering broad ranges of biofilm permeability (k_b) (from 10^{-15} m^2 to 10^{-7} m^2) and biofilm porosity (ε_b) (from 0.2 to 0.8). The overall permeability of the porous medium (k), the flow pathways and the overall/local pressure gradients were found to be highly dependent on β_r and k_b but were moderately impacted by ε_b when the biofilm levels were high and intermediate with $k_b > 10^{-11}$ m^2. When biofilm structures are well developed, simplified biofilm geometries, such as uniform coating and symmetric contact filling, can provide reasonable approximations of k.

1. Introduction

Bacteria can deposit and grow in nature and in engineered porous environments. After initial attachment to the surface of porous media, bacteria can excrete extracellular polymeric substances (EPS) and develop biofilms in the presence of moisture and nutrients. EPS play a significant role in the formation and structure of biofilms while protecting cells from environmental stresses and antimicrobial compounds (Benioug et al., 2017; Wang et al., 2019). The presence and growth of biofilms can modify the physical and chemical properties of porous media, such as surface roughness, chemical composition, hydrophobicity, and surface charge (Liu and Li, 2008; Redman et al., 2004; Walker et al., 2004). Moreover, the growth of biofilms in pore spaces and on grain surfaces changes the flow paths, pressure gradients, and flow velocities inside the porous medium (Carrel et al., 2018a; Nivala et al., 2012). However, it has been challenging to conduct controlled experiments and to mathematically simulate how biofilm formation and growth influence the hydrodynamics in porous media.

Traditionally, biofilms have been modeled as an impermeable domain in porous media. In such models, no water can enter biofilms, and contaminants can only enter biofilms via molecular diffusion (Bottero et al., 2013; Eberl et al., 2000; Peszynska et al., 2016; Pintelon et al., 2009; Taylor and Jaffé, 1990). Such a modeling approach is based on the assumption that the permeability of biofilms is similar to that of EPS, which are considered to have negligible permeability (Billings et al., 2015). However, some experimental studies, have demonstrated that the structure of biofilms is, in fact, very heterogeneous, with many pores and channels present (Flemming et al., 2019; Radu et al., 2012; Stoodley et al., 1994; Seymour et al., 2004), and the permeability of biofilms is higher than that of EPS (Jafari et al., 2018; Stoodley et al., 1994). A pioneering work (Seymour et al., 2004) used magnetic resonance measurements to sample flow within biofilms in porous media and provided evidence that the physical characteristics of biofilms, such as biofilm porosity and biofilm permeability, can strongly affect the flow dynamics and transport of solutes (Carrel et al., 2018; Davit et al., 2013). Another study (Thullner and Baveye, 2008) showed that only when biofilms were considered permeable could computer models reasonably predict the reduction in hydraulic conductivity caused by biofilms. Pintelon et al. (2012) conducted a systematic study on the influence of biofilm permeability on the overall biomass growth and showed that non-zero biofilm permeability should be included in all biofilm models. Deng et al. (2013) investigated the effect of permeable biofilms on macroscale and microscale flow in porous

* Corresponding author.
E-mail address: yli7@unl.edu (Y. Li).

https://doi.org/10.1016/j.watres.2020.116536
0043-1354/

media. They developed a model that predicted bulk permeability based on biofilm permeability and the biofilm volume ratio, which demonstrated a significant effect of biofilm permeability on shear stress distribution.

To produce an accurate model, it is crucial to correctly account for the effects of biofilms on hydrodynamics in porous media. Previous studies that considered biofilms to be permeable are mostly theoretical (Landa-Marbán et al., 2020; Pintelon et al., 2012; Qin and Hassanizadeh, 2015; Radu et al., 2012; Thullner and Baveye, 2008). A few experimental works studied permeable biofilms by imaging slices of bioclogged columns (Abbasi et al., 2018; Deng et al., 2013). Such images may not accurately represent the overall porous medium because only a small domain of the porous medium can be imaged for the columns, and the porous structure is highly random at the column scale. As columns are sometimes referred to as 'black boxes,' correlating the hydrodynamics of the pore space with biofilm distribution is very difficult and often inaccurate in such systems. Recently, microfluidic channels have been widely used to study biofilms in porous systems (Pousti et al., 2019; Subramanian et al., 2020) because they can provide a unique platform to control liquid flow at a scale comparable with typical biofilm dimensions in porous media. Although microfluidic channels can be useful tools to explore the spatiotemporal properties of biofilms in porous media (Valiei et al., 2012), most microfluidic-based biofilm studies have focused on qualitative observations of channels without porous media (Gottschamel et al., 2009; Kim et al., 2013; Mosier et al., 2012). Few works have attempted to mathematically simulate the influence of biofilms on the hydrodynamics in porous microfluidic channels based on experimental observations (Aufrecht et al., 2019; Singh and Olson, 2012).

Complicated biofilm structures evolve over time (Ghanbari et al., 2016; Hung et al., 2013), making it challenging to model the ever-evolving biofilms. Various approaches have been used to simplify the geometry of growing biofilms for modeling of the flow and transport in biofilm-clogged porous media (Ezeuko et al., 2011; Peszynska et al., 2016; Pintelon et al., 2009). In modeling studies, it has been a common practice to simplify biofilm geometries as a uniformly-coated layer on porous media (Abbasi et al., 2018; Cunningham and Mendoza-Sanchez, 2006). Some studies have proposed conceptual models in which biofilms mainly fill in the gaps between porous medium grains (Jaiswal et al., 2014; Vandevivere, 1995). These simplifications can reduce the time needed for image analysis and facilitate repeatability; however, these approaches are sometimes questioned for accuracy (Boudarel et al., 2018). Little is known about how different simplified biofilm geometries impact the permeability of porous media with evolving biofilm structures.

The goal of this study is to utilize a microfluidic channel to compare multiple approaches in modeling the impact of evolving biofilms on the flow in porous media. We aim to answer the following research questions: (1) how does biofilm growth impact the flow and overall permeability of porous media; (2) how do biofilm properties affect the flow fields, pressure gradient, and permeability of porous media; and (3) how well can simplified biofilm geometries pave the way in predicting the permeability of porous media?

In the present study, *E. coli* biofilms were grown in a microfluidic channel that was densely packed with uniform glass beads. Confocal microscope images were collected at three different biofilm growth stages in the microfluidic channel, and digitized images were used as inputs to simulate water flow in the biofilm-covered porous medium. We estimated the overall permeability of the biofilm-covered porous medium by solving the Navier-Stokes equations for flow in the pore spaces and a Forchheimer-corrected version of the Brinkman equation for flow inside biofilms. Biofilm properties, including biofilm porosity and biofilm permeability, were altered to examine their effects on the overall permeability of the porous medium. Finally, we evaluated two simplified models of biofilm geometries (i.e., uniform coating and symmetric contact filling) to pursue a possible abridged approach in modeling real biofilm geometries.

2. Materials and methods

2.1. Microfluidic channel and pumping system

A μ-slide I 0.6 Luer (ibidi GmbH, Martinsried/Munich, Germany) microfluidic channel (length = 50 mm, width = 5 mm, height = 0.6 mm) was packed with 0.5–0.6 mm diameter barium titanate solid glass microspheres (Cospheric, USA) with a high density of 4.16 g/cm^3. The μ-slide I 0.6 Luer microfluidic channels has a thin (180 µm) polymer coverslip bottom that has an optical quality comparable to glass (refractive index of 1.52 and Abbe number of 56) and is suitable for culture under flow and high-resolution microscopy. A computer-controlled pump system (ibidi GmbH, Martinsried/Munich, Germany) containing an ibidi air pump, fluidic unit, and perfusion set (length 50 cm, ID 0.8 mm, 10 mL reservoirs) was used to create a unidirectional and continuous medium flow. Fig. 1 illustrates the experimental setup. The packed channel and perfusion set were autoclaved before the experiments. After the removal of air bubbles, the flow rate and pressure were set at 1 mL/min and 17.4 mbar, respectively, via the ibidi PumpControl Software.

2.2. Biofilm cultivation

E. coli Strain K-12 MG1655 was used as the model bacteria in this study. A volume of 0.9 mL bacterial stock was added to 150 mL of autoclaved Luria-Bertani (LB) broth base solution and was then placed on a shaker for 22 h at 23 °C to reach the late-log phase. Then, the bacterial solution was pipetted into the packed channel under a biosafety cabinet, and the channel was put aside for 12 h to allow initial bacterial attachment. Next, the channel was connected to the pumping system under the biosafety cabinet, and 10 mL of 1/8 strength, autoclaved LB broth was used as the model flow in the microfluidic device under a unidirectional flow mode.

2.3. Experimental observations and image analysis

A Nikon A1R laser scanning confocal microscope (Nikon Corporation, Japan) was used to image the biofilms and porous medium inside the microfluidic channel. The confocal microscope images had 2343 × 2323 pixels with a resolution of 2.47 μm/pixel. More information is provided in the supplementary materials about the staining procedure and confocal laser scanning microscopy. In all the preliminary tests (data not shown), the biofilm growth was basically following the same trend of evolving except in the 1 cm adjacency of the inlet and outlet. Therefore, a 5 mm × 5.6 mm area (noted by a red rectangle in Figure S1) was chosen as the constant imaging frame for all further imaging sessions. This region of the microfluidic device was selected to accommodate the specifics of the microscopy method, avoid interference from the inlet/outlet of the device and ensure a balanced biofilm distribution. The reference point used for each imaging calibration is also shown in Figure S1.

Based on preliminary tests (data not shown), 15, 36 and 61 h of net feeding were required for biofilms to reach low, intermediate, and high levels in the channel, respectively. At these three time points (hereafter, referred to as day 1, 2, and 3), the microfluidic channel was taken off the line. FM 1–43 (Invitrogen

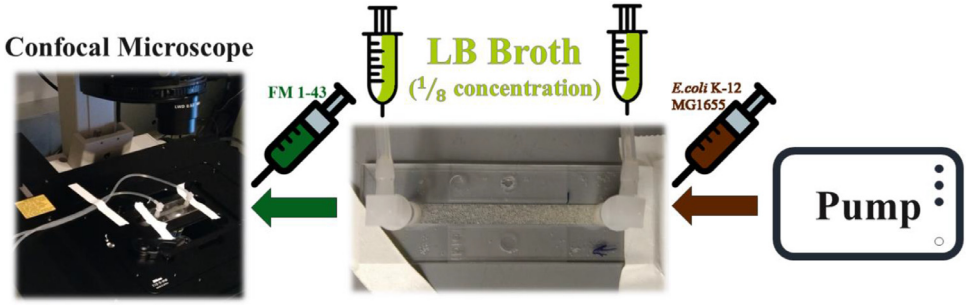

Fig. 1. The experimental setup; an ibidi pump system is used to create a volume-controlled flow in the microfluidic channel packed with glass beads, which is later visualized under a Nikon Ti2 confocal microscope.

Molecular Probes, USA), a lipophilic styryl dye with peak excitation and emission wavelengths of 510 and 626 nm, was used to stain the biofilms without affecting the viability of the cells (Bahlmann et al., 2001; Dahal et al., 2018).

The raw ND2 confocal microscopy images were analyzed using FIJI (https://fiji.sc/), which is an open-source image processing package based on ImageJ (1.52p, National Institutes of Health, USA). AutoCAD 2019 software (Autodesk, USA) was used to edit and prepare the geometry of the biofilm-covered porous medium as DXF files for computational fluid dynamics models. Finally, the porosity of the porous medium (φ) and the biofilm ratio (β_r) were estimated by the color thresholding feature of FIJI. φ was calculated as the percent ratio of the pore area to the total area, and β_r was defined as the percent ratio of the area covered by biofilm to the pore area.

2.4. Modeling

COMSOL Multiphysics 5.3a (COMSOL Inc., Sweden) was used to model the flow in the channel. A free and porous media flow (fp) interface was used to solve the Navier-Stokes equations Eqs. (1) and (2) in the fluid domain of the pores for a single-phase incompressible steady-state flow:

$$\rho(\boldsymbol{u}.\nabla)\mathbf{u} = \nabla.\left[-\mathrm{pI} + \mu\left(\nabla\mathbf{u} + (\nabla\mathbf{u})^T\right)\right] \tag{1}$$

$$\nabla.\boldsymbol{u} = 0 \tag{2}$$

where ρ is the density of the fluid (1000 kg/m^3), $\boldsymbol{u} = [u, v]$is the velocity vector for 2D simulation in the free flow domain, μ is the dynamic viscosity of water (0.001 Pa.s), and p is the pressure.

In this work, biofilms were considered a porous medium, and water flow through the biofilm domain was simulated simultaneously as the flow in the fluid domain of the pore space. The Reynolds number in this study was estimated as 15, which is higher than the upper limit of Darcy's law. In the case of a bioclogged porous medium, the growth of biofilm results in an alteration in flow conditions in sporadically distributed locations, and thus, a turbulent contribution of the resistance to flow must be considered. The flow of water inside the biofilm domain was therefore simulated using a Forchheimer-corrected version of the Brinkman equation Eqs. (3) and (4):

$$\frac{\mu}{k_b}\boldsymbol{u_f} = \nabla.\left[-\mathrm{pI} + \frac{\mu}{\varepsilon_b}\left(\nabla\mathbf{u_f} + \left(\nabla\mathbf{u_f}\right)^T\right)\right] - \beta_f\mathbf{u_f}\left|\mathbf{u_f}\right| \tag{3}$$

$$\nabla.\mathbf{u_f} = 0 \tag{4}$$

where ε_b is the biofilm porosity, k_b is the biofilm permeability (m^2), $\boldsymbol{u_f} = [u_f, v_f]$ is the Darcy flux vector, and β_f is the Forchheimer coefficient that is defined as Eq. (5):

$$\beta_f = \frac{\rho\varepsilon_b C_f}{\sqrt{k_b}} \tag{5}$$

where C_f is the dimensionless friction coefficient and is calculated by Eq. (6) as follows:

$$C_f = \frac{1.75}{\sqrt{150{\varepsilon_b}^3}} \tag{6}$$

The Brinkman equation accounts for fast-moving fluids in porous media with the kinetic potential from fluid velocity, pressure, and gravity driving the flow, which often describes transitions between slow flow in porous media that is governed by Darcy's law and fast flow in channels described by the Navier-Stokes equations. The Forchheimer equation amends the Brinkman equations with forces opposed to the flow direction, i.e., the momentum sink, which adds a correction for turbulent drag contributions. In COMSOL Multiphysics, this extra drag is applied as β_f.

A constant flowrate boundary condition was applied to the inlet of the domain, and a constant pressure boundary condition was applied to the domain outlet. A no-slip boundary condition was applied to the glass bead surfaces and walls of the channel. A physics-controlled mesh sequence type with extra fine element sizes discretized the entire computational domain into approximately 350,000 mesh elements. At the end of the simulation, the average pressures of the inlet and outlet were calculated based on the simulated pressure distribution. The difference between the inlet and outlet average pressures was used to estimate the overall permeability of the porous channel based on Darcy's law (Eq. (7)):

$$k = \frac{\mu LQ}{A\Delta p} \tag{7}$$

where k is the permeability of the porous medium (m^2), L is the length between the inlet and outlet boundaries (m), Q is the discharge through the porous medium (m^3/s), and A is the cross-sectional area (m^2). In the simulations in this study, Q was 1.67×10^{-8} (m^3/s) as set in the experiments by the pumping system computer and L was 5.6 mm.

Biofilm properties, including k_b and ε_b, are critical parameters to model water flow through the biofilm domain. Determining the exact values of k_b and ε_b is challenging due to the heterogeneity of biofilm structures and technical limitations. A wide variety of values for k_b and ε_b have been reported in the literature. For instance, (Picioreanu et al., 2018) considered values of 0.6 and 10^{-15} m^2 for ε_b and k_b, respectively. Deng et al. (2013) used a range of 0.6 to 0.9 for ε_b while changing the value of k_b from 10^{-15} to 0.5×10^{-9} m^2. In this work, we also considered a wide range of ε_b (from 0.2 to 0.8) and k_b (from 10^{-15} m^2 to 10^{-7} m^2) values to evaluate how these biofilm properties influence the flow and permeability.

Due to the small size of the microfluidic channel and very low range of pressure, measuring the physical pressure drop before and after the microfluidic channel was impossible. However, the intrinsic permeability of the domain (k_i) was estimated using the Kozeny-Carman equation (Eq. (8)):

$$k_i = \frac{\varphi^3 d^2}{180(1-\varphi)^2} \tag{8}$$

where d is the average diameter of the beads that is 0.5 mm. With an average φ of 0.3 for the porous media, k_i is estimated as 7.65×10^{-11} m^2. Later in Section 3.1, Table 1, the estimated values of k_i for each day is presented alongside the modeled k of the porous domain without biofilms.

2.5. Simplified biofilm geometries

In this study, two geometry simplification approaches, namely, "uniform coating" and "symmetric contact filling," were evaluated for their ability to approximate the equivalent permeability of biofilm-covered porous media. The β_r values in the segmented simplified models were set at the same level as those determined experimentally from confocal images. After simplifying the biofilm shapes and distribution, water flow in a porous medium with simplified biofilm geometries was simulated using the same modeling approach described above.

In the uniform coating approach, biofilms were distributed as a uniform layer on each bead while maintaining the same β_r value obtained in the experiments on each day. For this purpose, the area covered by biofilms was divided by the number of beads in each image. The resulting value for each day was then used as a reference to manually create the outer layer on each bead based on the size of that bead, which was then scaled up via AutoCAD by a factor of 1.00687, 1.03871, and 1.14697 for day 1, day 2, and day 3 images, respectively. It should be noted that for day 1, the uniform biofilm coating on the beads had a negligible thickness.

The symmetric contact filling approach assumes that the biofilms are formed in contact areas of the porous medium that are narrower and have higher local flowrates. Based on the porous medium geometry, 0.035 mm was set as the threshold for the distance of beads in contact areas. The β_r on each day obtained from the experiments was symmetrically distributed between the contact areas in the porous medium that were closer than 0.035 mm.

3. Results and discussion

3.1. Experimental domain analysis

Fig. 2 presents the biofilm levels on days 1, 2, and 3 in the same imaging area of the microfluidic channel. Figs. 2(a) and (b) show the brightfield and fluorescence views, and Fig. 2(c) shows the final digitized and segmented images obtained with AutoCAD and FIJI. It should be noted that the flow direction was from right to left. As shown in Fig. 2, the biofilm levels increased over the course of 3 days. In this study, biofilm attached to glass beads and biofilm in the void space were not differentiated in the model and were assumed to have the same permeability and porosity. Table 1 summarizes the β_r values and porous media characteristics analyzed with FIJI, in addition to the values of k_i from the Kozeny-Carman equation and k of the modeled domain without biofilms. β_r increased from 2.7% on day 1 to 17.6% and 55.2% on day 2 and day 3, respectively, while the porosity of the system remained nearly constant, with a less than 5% difference. Based on these values of φ, k_i was estimated using the Kozeny-Carman equation. Interestingly, the k values we got from modeling the domain in each day without the presence of biofilm, are very close to the estimated values of k_i by the Kozeny-Carman equation as shown in Table 1.

Table 1
Porous medium characteristics.

Time	Total area of the image (mm^2)	Area covered by the beads (mm^2)	Area covered by biofilm (mm^2)	Area covered by fluid (mm^2)	φ (%)	β_r (%)	k_i (*Kozy-Carman*)(m^2)	k without biofilms (m^2)
Day 1	28.115	19.434	0.233	8.448	30.8	2.7	8.47E-11	3.79E-11
Day 2	27.896	20.474	1.305	6.117	26.6	17.6	4.85E-11	1.23E-11
Day 3	28.008	19.028	4.961	4.020	32.1	55.2	9.96E-11	4.71E-11

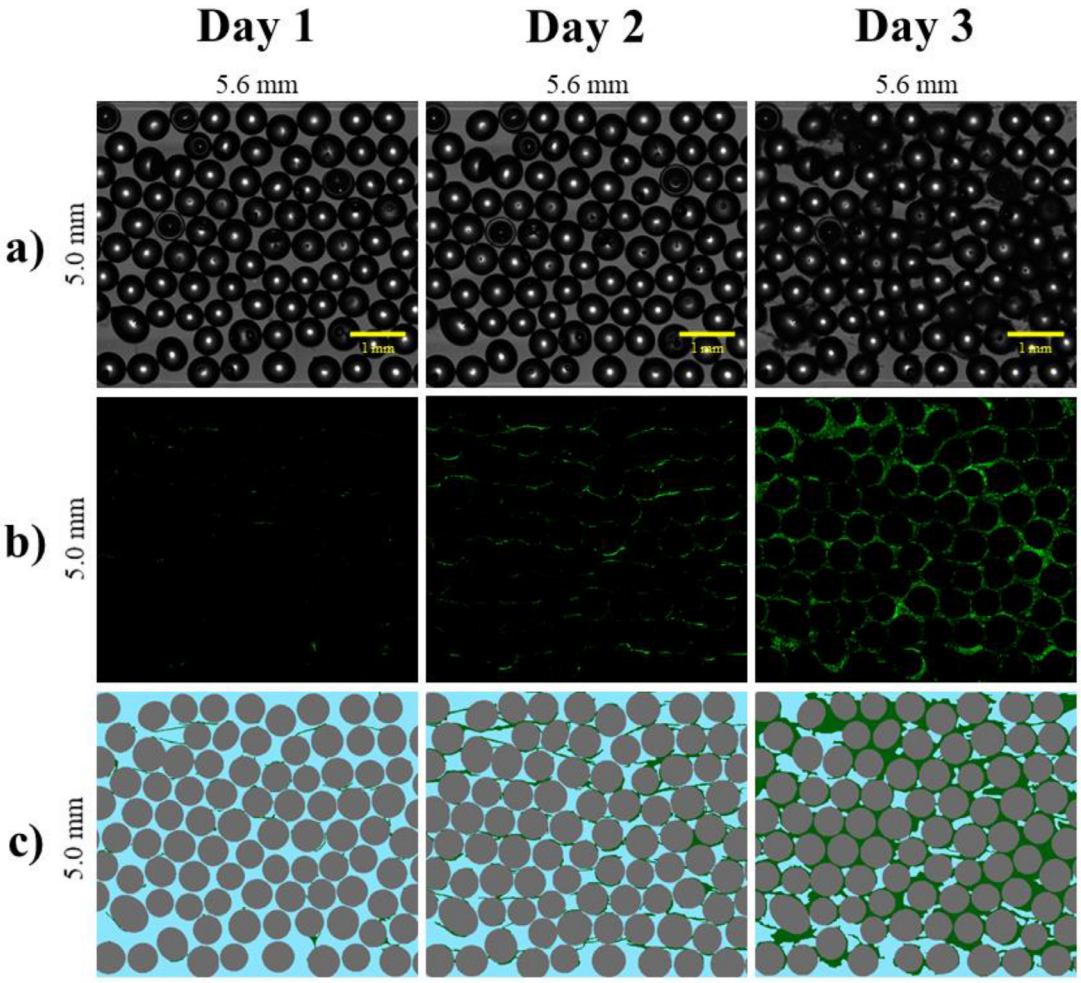

Fig. 2. Images of the microfluidic channel under brightfield microscopy (a) and fluorescence microscopy (b); segmented images (c) based on the fluorescence images.

3.2. Modeling results

3.2.1. Simulated flow fields

Fig. 3 shows the field of flow velocity normalized by the maximum velocity of each simulation in the porous medium with different biofilm levels. The simulations were for three k_b values of 10^{-9} m^2, 10^{-12} m^2, and 10^{-15} m^2, while ε_b remained at 0.6. It should be noted that the quantitative analysis of flow pathways is beyond the scope of this paper. However, we show that the flow paths at different growth stages depend on the biofilm properties.

When k_b was 10^{-15} m^2, the biofilm was nearly impermeable. Because liquid hardly flowed through the thick biofilm structures, it had to change flow pathways. When the k_b value increased to 10^{-12} m^2, water could still not easily flow through the biofilm structures, but the flow pathways changed. In contrast, when the k_b value was increased to 10^{-9} m^2, biofilms nearly lost their resistance to water penetration and showed a minimal effect on the flow.

The impacts of biofilms on the flow paths in bioclogged porous media have been discussed in the literature (Franklin et al., 2019; Morales et al., 2010; Rubol et al., 2014). In this regard, Bottero et al. (2013) investigated the dynamics of preferential flow paths in porous media with development of biofilms. Their results showed that under constant liquid flow at the inlet, a quasi-steady state permeability was reached, and they concluded that shear forces alone could lead to the formation of preferential flow paths that maintain their location in time. Although they accounted for attachment, growth, decay, lysis, and detachment of biofilms, all their results concerning flow paths and solute transport were based on assignment of a no-slip wall to biofilms in their model based on a paper published in 1991 (Fowler and Robertson, 1991) suggesting that the permeability of biofilms is in the range of 10^{-16} m^2 (i.e., impermeable). Our results demonstrate that the flow paths at different growth stages clearly depend on the biofilm permeability. Qin and Hassanizadeh (2015) reported that biofilm permeability had a large impact on biofilm growth and flow pathways when the biofilm level was high but had minimal impact at a low biofilm level. Qin and Hassanizadeh (2015) used a pore-network model in their simulation, which largely simplified the geometry in pore spaces even though they assigned a non-zero permeability to the biofilms. In our simulations, we observed significant impacts of biofilm permeability on the flow pathways, even with a β_r of 2.7% (i.e., day 1). The impact was intensified under higher biofilm coverage (i.e., days 2 and 3). Moreover, our simulations incorporated real biofilm geometries in the porous medium. Therefore, our approach is more sensitive for capturing the impact of biofilms on flow pathways.

3.2.2. Pressure distribution

Fig. 4 depicts the local pressure gradient normalized by the maximum pressure in each simulation with different biofilm levels. The overall pressure difference in the 5 mm $\times$ 5.6 mm area is presented in Figure S3. In all simulations, normalized pressure was higher at the inlet (right) than at the outlet (left). The overall

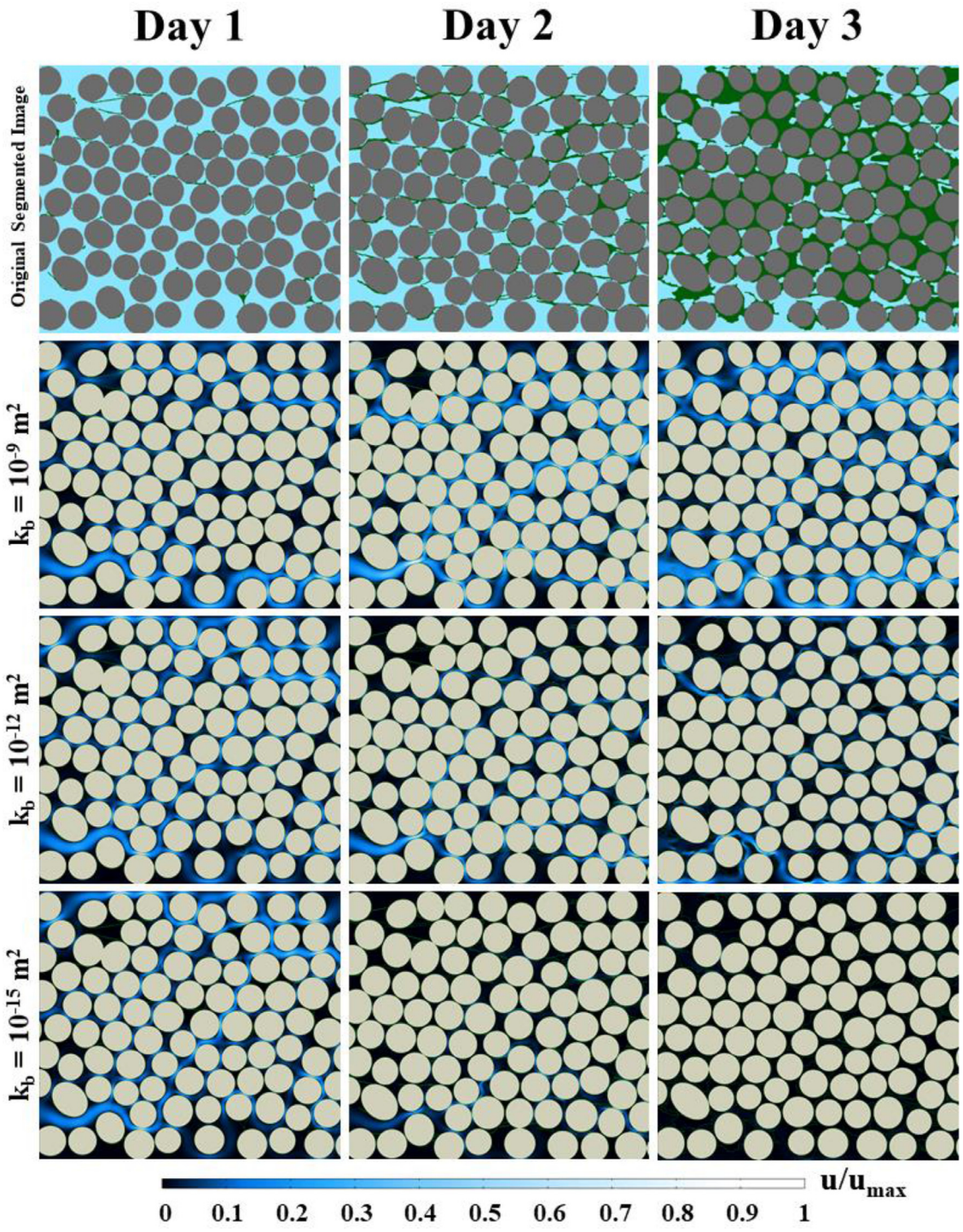

Fig. 3. The sensitivity of flow fields to the different k_b values used in modeling via COMSOL Multiphysics for different biofilm levels (ε_b was kept constant at 0.6).

pressure gradient is higher on day 3 for all three k_b values compared to earlier days. On each day, the overall pressure gradient is higher with lower k_b values. These results are expected according to Darcy's law, and reflected by higher k on day 1 than the other days, and higher k with higher k_b values. Furthermore, local pressure differences around and inside biofilms lead to changes in shear stress that eventually could play a significant role in biofilm detachment. In Fig. 4, a fixed area (designated with red) is enlarged to illustrate local pressure differences under various biofilm permeabilities. The areas were picked based on the amount and the location of the biofilm to better illustrate how the local pressure gradient in evolving biofilms is affected by β_r and k_b.

Fig. 4 illustrates the pressure gradient on day 1 across a biofilm structure that bridged two glass beads under different k_b values. When k_b was 10^{-15} m^2, the nearly impermeable biofilm significantly affected the local pressure in biofilm adjacencies. The pressure dropped almost five times across the biofilm, and the pressure gradient inside the biofilm was very high. When k_b was increased to 10^{-12} m^2, the pressure dropped gradually inside the biofilm structures. When the k_b value reached 10^{-9} m^2, the biofilm showed a minimal effect on the pressure distribution. Interestingly,

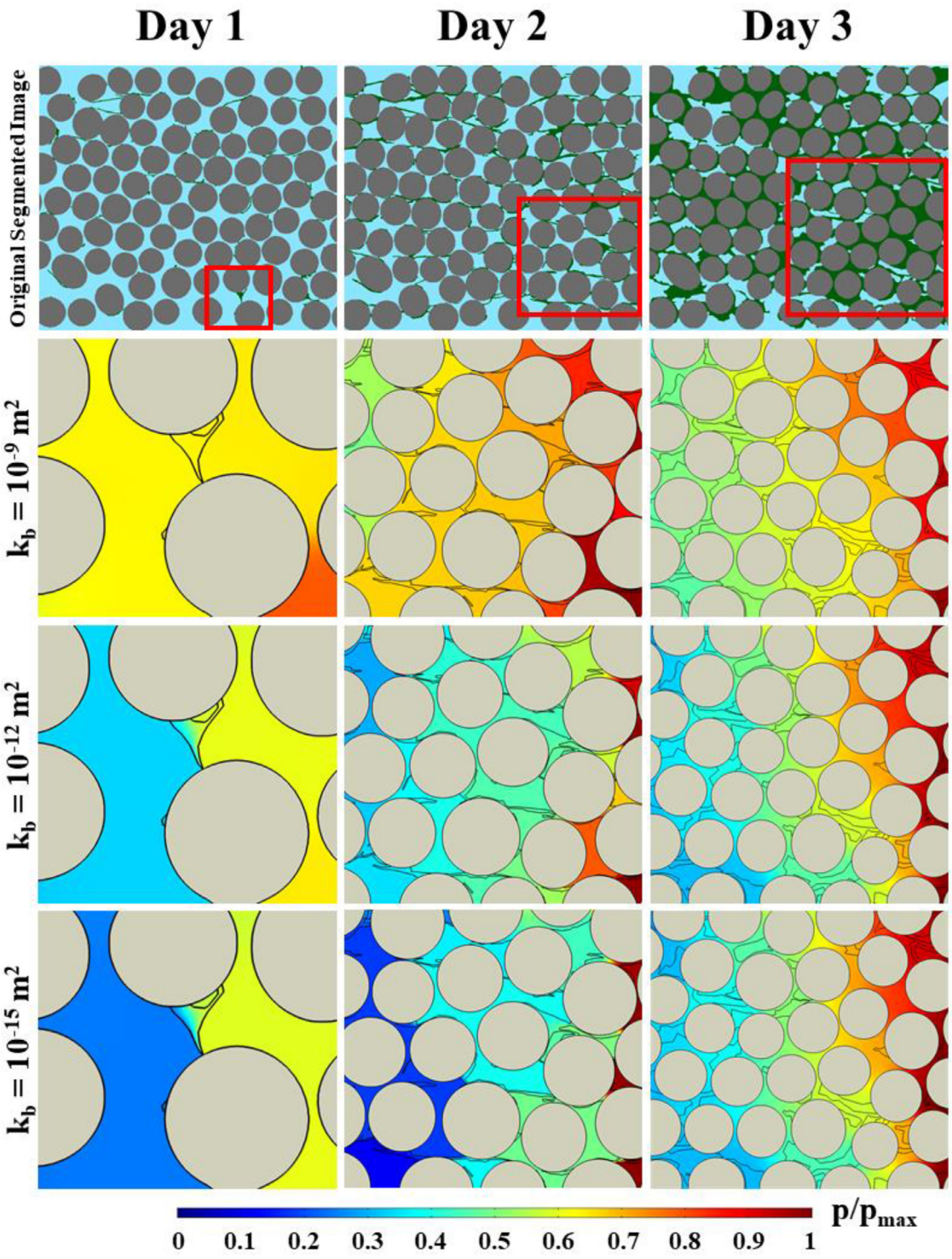

Fig. 4. The sensitivity of local pressure gradients to the different k_b values used in modeling with COMSOL Multiphysics for different biofilm levels (ε_b was kept constant at 0.6).

as the biofilm grew thicker on day 2 and day 3, the pressure inside the biofilm was more gradually attenuated than it was on day 1. These simulations explain why thinner biofilms that are bridging the particles in a porous medium in the early stages of biofilm development are more susceptible to detachment due to abrupt alterations in local pressure and shear stress.

For all three days, the pressure drops in the designated areas were clearly impacted by k_b values. On day 1 and day 2, when k_b values decreased from 10^{-9} m^2 to 10^{-15} m^2, the pressure gradient in the designated areas increased substantially. In day 3, large pressure drops in the vicinity of biofilms was observed and the pressure gradient increased when k_b decreased from 10^{-9} m^2 to 10^{-12} m^2; however, further decreasing the k_b from 10^{-12} m^2 to 10^{-15} m^2 did not significantly affect the normalized pressure drop and distribution. This is because the denser and more evenly distributed biofilms present on day 3 had already clogged most pore spaces and allowed very little water flow to permeate; thus, the further decrease in the k_b value did not have a significant impact on wa-

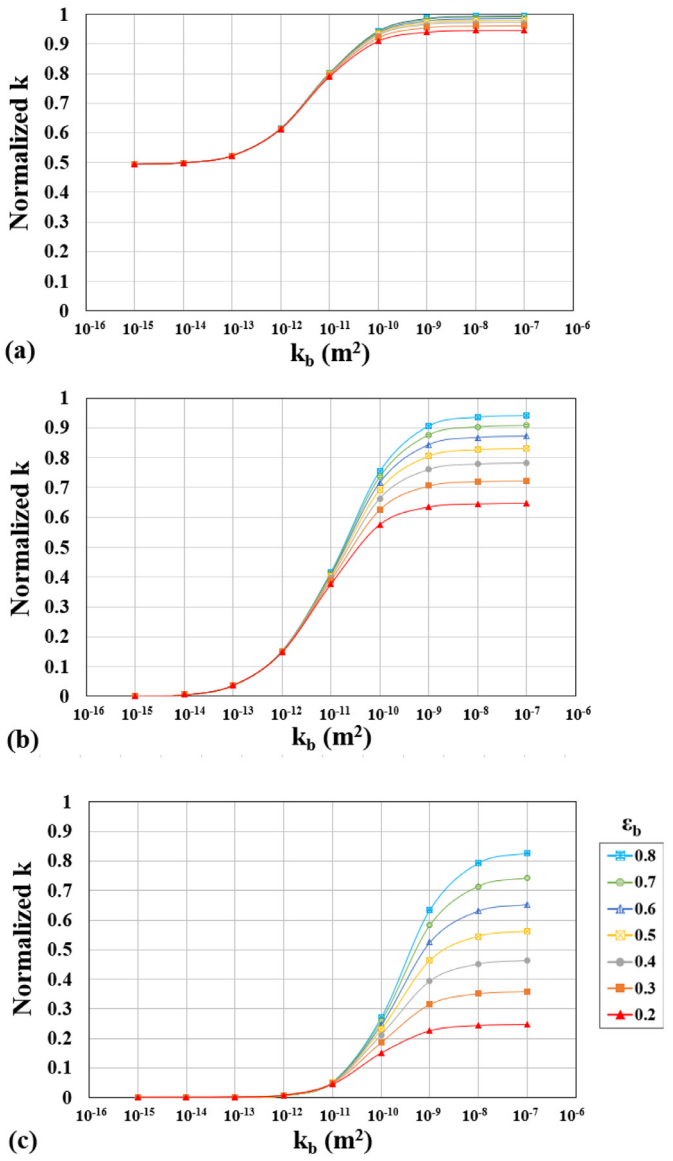

Fig. 5. The sensitivity of normalized k to k_b and ε_b for different biofilm levels on days 1, 2 and 3 of the modeled experiments.

ter flow. Our results suggest that β_r and k_b are crucial parameters to consider when predicting the behavior of biofilms, such as detachment, in porous systems.

3.2.3. Impacts of biofilm properties on the overall porous medium permeability

Fig. 5 illustrates the sensitivity of the overall permeability k to biofilm permeability k_b. The very left points in all the graphs in Fig. 5 represent nearly impermeable biofilms (k_b=10^{-15} m^2), and as k_b increases, the biofilm becomes more permeable. The highest k_b value of 10^{-7} m^2 indicates very permeable biofilms. For each simulation, the final simulated values of k were normalized to the k of the original porous medium without any biofilms.

As shown in Fig. 5, normalized k was very sensitive to changes in k_b. For all three levels, the overall permeability was the smallest when biofilms were impermeable. On day 1, when biofilms were considered nearly impermeable (10^{-15} m^2), the normalized k value was reduced to only half of the original k without the biofilm presence. On days 2 and 3, the normalized k value approached zero when biofilms were defined as impermeable. As biofilm permeability increased, the overall permeability for all three biofilm ratios also increased. As an example, the impacts of k_b on normalized k are elaborated with a fixed ε_b value of 0.6. In the lowest biofilm level (day 1), normalized k was reduced from 0.98 to 0.49 when k_b decreased from 10^{-7} m^2 to 10^{-15} m^2, respectively. On day 2 with an intermediate biofilm level, for the fixed ε_b value of 0.6, normalized k dropped from a maximum of 0.87 for a k_b of 10^{-7} m^2 to a minimum of 0.0006 for a k_b of 10^{-15} m^2. On day 3 with a high biofilm level, the effect of β_r in the pore space outweighed the effect of k_b because the porous medium was very clogged. Even for the highly permeable biofilms with k_b values of 10^{-7} m^2, the maximum normalized k value was only 0.65 for the fixed ε_b value of 0.6.

In this study, we showed that ε_b had a minimal effect on k when biofilm levels were low in the system and when k_b was also low. Fig. 5 shows when the k_b values were smaller than 10^{-11} m^2, changes in ε_b values in the range of 0.2 to 0.8 had a negligible effect on normalized k in all three biofilm levels. However, when the k_b values were higher than 10^{-11} m^2, the effect of ε_b became obvious, especially on days 2 and 3. For instance, on day 2, with a k_b of 10^{-9} m^2, the normalized k changed from 0.63 to 0.9 for ε_b values of 0.2 and 0.8, respectively. Under the same conditions, the difference became even greater on day 3, when normalized k could be as low as 0.22 for an ε_b of 0.2 and as high as 0.63 for an ε_b of 0.8. However, a previous study (Deng et al., 2013) claimed that k is almost insensitive to ε_b and neglected the effect of ε_b in the development of a predictive equation for k. We believe the discrepancy between our study and that work is due to different modeling approaches, domain sizes, and ranges of k_b and ε_b tested. That work (Deng et al., 2013) used the Brinkman equation for the biofilm domain, while we used the Forchheimer-corrected version of the Brinkman equation. Additionally, they sampled a 0.45 mm × 0.45 mm domain from a column study, while our simulation domain was 5 mm × 5.6 mm. Moreover, the ranges of k_b and ε_b were 10^{-15} to 5 × 10^{-9} m^2 and 0.6 to 0.9 in that study, while in our study they were 10^{-15} to 10^{-7} m^2 and 0.2 to 0.9, respectively. The effect of ε_b in our simulation can be explained by Eq. (3). Decreasing k_b gradually drives the equation towards Darcy's law, in which ε_b is typically not a very sensitive parameter, while with an increasing k_b, the equation gradually moves towards the steady-state form of the Navier-Stokes equations. Determining the exact values of k_b and ε_b are beyond the scope of this paper. However, the sensitivity of flow to ε_b in porous media highly depends on β_r and k_b. Depending on the experimental conditions, biofilms may form structures with different porosities and permeabilities. The wide ranges and various combinations of k_b and ε_b used in the present study, which resulted in significantly different permeabilities, flow fields, and pressure distributions, illustrate the importance of accurate determination of biofilm properties for modeling the hydrodynamics of biofilm-covered porous media at different stages.

We successfully generated a series of realistic 2D models of porous media with evolving permeable biofilms based on confocal images of continuous biofilm growth in porous media inside a microfluidic channel. In most available theoretical studies, biofilms are arbitrarily distributed in pore spaces or on grains, and small modeling domains are typically used (Cunningham and Mendoza-Sanchez, 2006; Qin and Hassanizadeh, 2015; Tang and Liu, 2017). The use of digitized confocal images allowed us to consider actual biofilm geometries in simulating the flow and permeability of porous media. Deng and co-workers (Deng et al., 2013) generated 2D models of biofilm-filled porous media based on confocal images. However, their domain size was only 0.45 mm × 0.45 mm with 1024 × 1024 pixels, and the domain contained 20 glass beads (whole or partial) with a size of 0.1 – 0.15 mm diameter. In our study, the domain size is 5 mm × 5.6 mm with 2343 × 2323 pix-

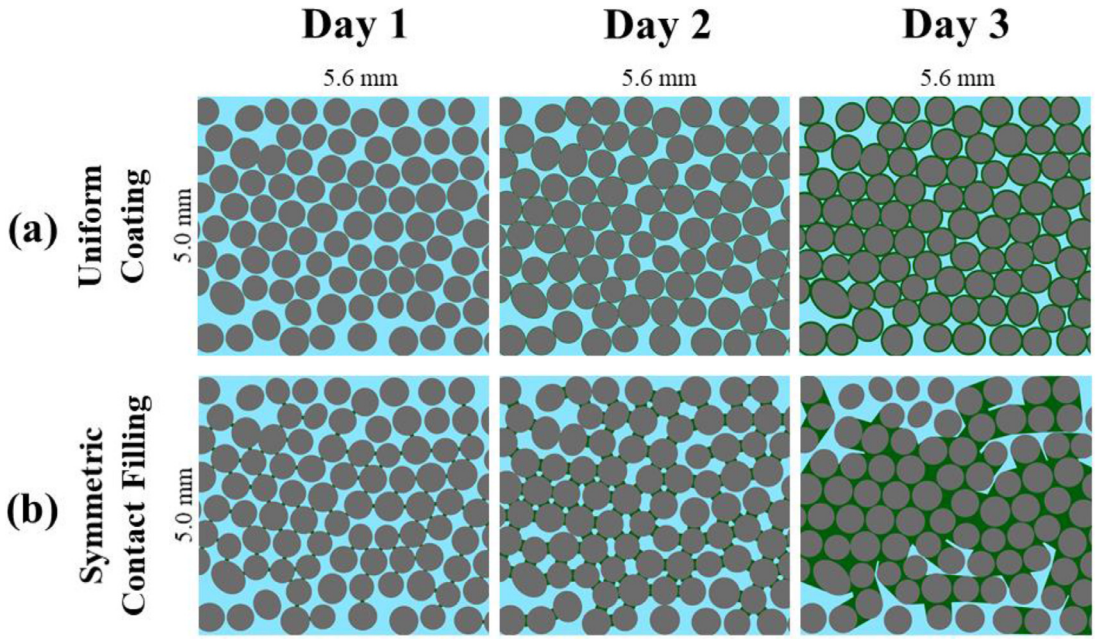

Fig. 6. Simplified biofilm geometries and distribution via (a) uniform coating, and (b) symmetric contact filling.

els and the domain has 93 glass beads with an average size of 0.5 mm.

Similar to the limitation of any other 2D models, our model cannot simulate the impact of biofilm on flow in the vertical dimension. However, our images were based on MaxIP pictures that included all biofilms in the entire vertical space of the channel, such that the complexity of biofilm morphology in the vertical direction was somewhat preserved throughout the whole domain.

3.3. Simplified biofilm geometries

Fig. 6 presents segmented images with simplified biofilm geometries (i.e., uniform coating and symmetric contact filling). These images were compared with the digitized images of real biofilms to ensure that β_r values were the same for all time points under both simplification approaches.

Fig. 7 compares the normalized k, simulated using the simplified biofilm geometries, and modeled experiments in the full range of k_b for four ε_b values. Additional simulation results based on the simplified geometries for a full range of k_b and ε_b are provided in Figure S4. On day 1, with low biofilm levels in the system, the uniform coating was so thin that the impacts of biofilm on k were negligible. Therefore, the uniform coating method cannot be used for low biofilm ratios. Fig. 7 also clearly indicates that the symmetric contact filling approach largely underestimated k for the full range of k_b and all four ε_b values, although the discrepancy seems reduced at the higher k_b and ε_b values. Based on this, the symmetric contact filling approach was not accurate in approximating the actual experiments on day 1 and thus is not effective in examining low biofilm levels. The results for the intermediate biofilm level on day 2 were very similar between the uniform coating and the symmetric contact filling simplification scenarios. Both simplified geometries underestimated the normalized k over the range of k_b for all four ε_b values. The discrepancy was higher at lower ε_b values. When ε_b was as high as 0.8, the normalized k values estimated from these simplified geometries were approximately 90% of the normalized k estimated from actual experiments.

For the high biofilm levels on day 3, estimations from both simplified geometries significantly improved compared to those for days 1 and 2. The symmetric contact filling approach slightly overestimated the normalized k values. The discrepancy seemed higher at higher k_b and lower ε_b values. For the highest k_b of 10^{-7} m^2, the absolute error of the symmetric contact filling approach was 0.11, 0.09, 0.07, and 0.04 for ε_b values of 0.2, 0.4, 0.6, and 0.8, respectively. On the other hand, the uniform coating method slightly underestimated the normalized k values but with less discrepancy. Similar to the symmetric contact filling approach, this method produced higher discrepancies at higher k_b and lower ε_b values. For the highest k_b of 10^{-7} m^2, the absolute error of the uniform coating approach was 0.04, 0.04, 0.04 and 0.02 for ε_b values of 0.2, 0.4, 0.6 and 0.8, respectively.

These data indicate that uniform coating and symmetric contact filling, could provide a reasonable approximation of k when the biofilm levels are high in porous media. With high biofilm levels, the uniform coating method produced acceptable estimates for all combinations of ε_b and k_b values, and the symmetric contact filling approach seemed to be more accurate when ε_b values were higher. These findings also emphasize the importance of accurately determining biofilm properties (such as ε_b and k_b) to simplify the modeling and design of porous systems.

4. Conclusions

This study integrated lab experiments and mathematical modeling to better understand the effects of biofilm formation, growth, and properties on the hydrodynamics of porous media inside a microfluidic channel. Furthermore, we evaluated the possibility of using two simplified biofilm geometries (uniform coating and symmetric contact filling) to more effectively estimate the overall permeability of biofilm-clogged porous media. The main conclusions of this study are summarized as follows:

- The presence, growth, and properties (k_b and ε_b) of biofilms clearly affect the flow fields and overall/local pressure gradients. The permeability of porous media is highly dependent on k_b, although with high biofilm levels, the effect of β_r outweighs the effect of k_b. The effect of ε_b cannot be neglected in modeling intermediate and high biofilm levels and becomes more

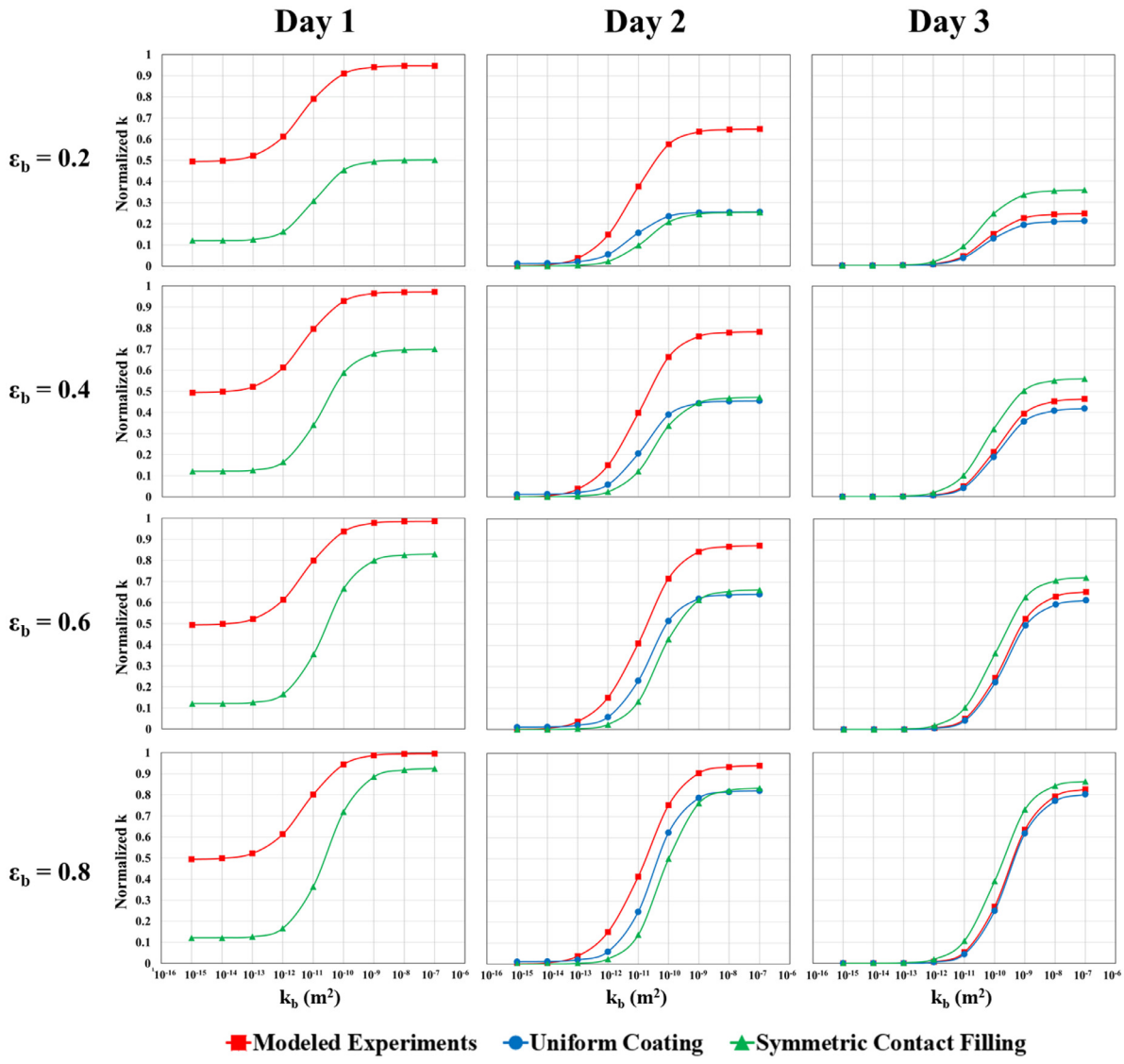

Fig. 7. Simulated k vs. k_b for modeled experiments, uniform coating, and symmetric contact filling with four ε_b values and different biofilm levels on days 1, 2 and 3 .

obvious when the biofilm is considered to be more permeable ($k_b > 10^{-11}$ m^2).

- Neither the uniform coating approach nor the symmetric contact filling approach could predict the k accurately for the low biofilm level on day 1 or the intermediate biofilm level on day 2, although the discrepancies decreased on day 2, especially with higher ε_b values. However, both approaches provided improved estimation of k for the high biofilm level on day 3. Thus, simplifying the biofilm geometries by symmetric contact filling and uniform coating methods for permeability studies in porous media can be implemented if the biofilm levels are high in the system.
- The results from the modeled experiments and simplified biofilm geometries demonstrate the importance of accurate determination of biofilm properties, such as k_b and ε_b, for permeability modeling and design purposes.

Declaration of Competing Interest

The authors declare that they have no known competing financial interests or personal relationships that could have appeared to influence the work reported in this paper.

Acknowledgments

The authors are thankful to the National Science Foundation (NSF) (award number CBET-1511941 and CBET-1836799) and Dr. You (Joe) Zhou from Morrison Microscopy Core Research Facility at the University of Nebraska-Lincoln for all his help in microscopy.

Supplementary materials

Supplementary material associated with this article can be found, in the online version, at doi:10.1016/j.watres.2020.116536.

References

Abbasi, B., Ta, H.X., Muhunthan, B., Ramezanian, S., Abu-Lail, N., Kwon, T.-H., 2018. Modeling of permeability reduction in bioclogged porous sediments. J. Geotech. Geoenviron. Eng. 144, 04018016. doi:10.1061/(ASCE)GT.1943-5606.0001869.

Aufrecht, J.A., Fowlkes, J.D., Bible, A.N., Morrell-Falvey, J., Doktycz, M.J., Retterer, S.T., 2019. Pore-scale hydrodynamics influence the spatial evolution of bacterial biofilms in a microfluidic porous network. PLoS ONE 14, e0218316. doi:10.1371/journal.pone.0218316.

Bahlmann, K., Jakobs, S., Hell, S.W., 2001. 4Pi-confocal microscopy of live cells. Ultramicroscopy 87, 155–164. doi:10.1016/S0304-3991(00)00092-9.

Benioug, M., Golfier, F., Oltéan, C., Buès, M.A., Bahar, T., Cuny, J., 2017. An immersed boundary-lattice Boltzmann model for biofilm growth in porous media. Adv. Water Resour. 107, 65–82. doi:10.1016/j.advwatres.2017.06.009.

Billings, N., Birjiniuk, A., Samad, T.S., Doyle, P.S., Ribbeck, K., 2015. Material properties of biofilms—a review of methods for understanding permeability and mechanics. Reports Prog. Phys. 78, 036601. doi:10.1088/0034-4885/78/3/036601.

Bottero, S., Storck, T., Heimovaara, T.J., van Loosdrecht, M.C.M., Enzien, M.V., Picioreanu, C., 2013. Biofilm development and the dynamics of preferential flow paths in porous media. Biofouling 29, 1069–1086. doi:10.1080/08927014.2013.828284.

Boudarel, H., Mathias, J.D., Blaysat, B., Grédiac, M., 2018. Towards standardized mechanical characterization of microbial biofilms: analysis and critical review. npj Biofilms Microbiomes 4. doi:10.1038/s41522-018-0062-5.

Carrel, Maxence, Morales, V.L., Beltran, M.A., Derlon, N., Kaufmann, R., Morgenroth, E., Holzner, M., 2018a. Biofilms in 3D porous media: delineating the influence of the pore network geometry, flow and mass transfer on biofilm development. Water Res. 134, 280–291. doi:10.1016/j.watres.2018.01.059.

Carrel, M., Morales, V.L., Dentz, M., Derlon, N., Morgenroth, E., Holzner, M., 2018b. Pore-scale hydrodynamics in a progressively bioclogged three-dimensional porous medium: 3-D particle tracking experiments and stochastic transport modeling. Water Resour. Res. 54, 2183–2198. doi:10.1002/2017WR021726.

Cunningham, J.A., Mendoza-Sanchez, I., 2006. Equivalence of two models for biodegradation during contaminant transport in groundwater. Water Resour. Res. 42, 1–10. doi:10.1029/2005WR004205.

Dahal, D., Ojha, K.R., Alexander, N., Konopka, M., Pang, Y., 2018. An NIR-emitting ESIPT dye with large stokes shift for plasma membrane of prokaryotic (E. coli) cells. Sensors Actuators B Chem 259, 44–49. doi:10.1016/j.snb.2017.12.041.

Davit, Y., Byrne, H., Osborne, J., Pitt-Francis, J., Gavaghan, D., Quintard, M., 2013. Hydrodynamic dispersion within porous biofilms. Phys. Rev. E 87, 012718. doi:10.1103/PhysRevE.87.012718.

Deng, W., Cardenas, M.B., Kirk, M.F., Altman, S.J., Bennett, P.C., 2013. Effect of permeable biofilm on micro- and macro-scale flow and transport in bioclogged pores. Environ. Sci. Technol. 47, 11092–11098. doi:10.1021/es402596v.

Eberl, H., Picioreanu, C., Heijnen, J., van Loosdrecht, M.C, 2000. A three-dimensional numerical study on the correlation of spatial structure, hydrodynamic conditions, and mass transfer and conversion in biofilms. Chem. Eng. Sci. 55, 6209–6222. doi:10.1016/S0009-2509(00)00169-X.

Ezeuko, C.C., Sen, A., Grigoryan, A., Gates, I.D., 2011. Pore-network modeling of biofilm evolution in porous media. Biotechnol. Bioeng. 108, 2413–2423. doi:10.1002/bit.23183.

Flemming, H.-.C., Szewzyk, U., Griebe, T., 2019. Biofilms: Investigative Methods and Applications, 1st Editio CRC Press.

Fowler, J.D., Robertson, C.R., 1991. Hydraulic permeability of immobilized bacterial cell aggregates. Appl. Environ. Microbiol. 57, 102–113. doi:10.1128/AEM.57.1.102-113.1991.

Franklin, S., Vasilas, B., Jin, Y., 2019. More than meets the dye: evaluating preferential flow paths as microbial hotspots. Vadose Zo. J. 18, 1–8. doi:10.2136/vzj2019.03.0024.

Ghanbari, A., Dehghany, J., Schwebs, T., Müsken, M., Häussler, S., Meyer-Hermann, M., 2016. Inoculation density and nutrient level determine the formation of mushroom-shaped structures in Pseudomonas aeruginosa biofilms. Sci. Rep. 6, 32097. doi:10.1038/srep32097.

Gottschamel, J., Richter, L., Mak, A., Jungreuthmayer, C., Birnbaumer, G., Milnera, M., Brückl, H., Ertl, P., 2009. Development of a disposable microfluidic biochip for multiparameter cell population measurements. Anal. Chem. 81, 8503–8512. doi:10.1021/ac901420u.

Hung, C., Zhou, Y., Pinkner, J.S., Dodson, K.W., Crowley, J.R., Heuser, J., Chapman, M.R., Hadjifrangiskou, M., Henderson, J.P., Hultgren, S.J., 2013. Escherichia coli biofilms have an organized and complex extracellular matrix structure. MBio 4, 1–10. doi:10.1128/mBio.00645-13.

Jafari, M., Desmond, P., van Loosdrecht, M.C.M., Derlon, N., Morgenroth, E., Picioreanu, C., 2018. Effect of biofilm structural deformation on hydraulic resistance during ultrafiltration: a numerical and experimental study. Water Res. 145, 375–387. doi:10.1016/j.watres.2018.08.036.

Jaiswal, P., Al-Hadrami, F., Atekwana, E.A., Atekwana, Eliot A., 2014. Mechanistic models of biofilm growth in porous media. J. Geophys. Res. Biogeosci. 119, 1418–1431. doi:10.1002/2013JG002440.

Kim, J., Kim, H.-.S., Han, S., Lee, J.-.Y., Oh, J.-.E., Chung, S., Park, H.-.D., 2013. Hydrodynamic effects on bacterial biofilm development in a microfluidic environment. Lab. Chip 13, 1846. doi:10.1039/c3lc40802g.

Landa-Marbán, D., Bødtker, G., Kumar, K., Pop, I.S., Radu, F.A., 2020. An upscaled model for permeable biofilm in a thin channel and tube. Transp. Porous Media 132, 83–112. doi:10.1007/s11242-020-01381-5.

Liu, Y., Li, J., 2008. Role of pseudomonas aeruginosa biofilm in the initial adhesion, growth and detachment of escherichia coli in porous media. Environ. Sci. Technol. 42, 443–449. doi:10.1021/es071861b.

Morales, V.L., Parlange, J.-.Y., Steenhuis, T.S., 2010. Are preferential flow paths perpetuated by microbial activity in the soil matrix? a review. J. Hydrol. 393, 29–36. doi:10.1016/j.jhydrol.2009.12.048.

Mosier, A.P., Kaloyeros, A.E., Cady, N.C., 2012. A novel microfluidic device for the in situ optical and mechanical analysis of bacterial biofilms. J. Microbiol. Methods 91, 198–204. doi:10.1016/j.mimet.2012.07.006.

Nivala, J., Knowles, P., Dotro, G., García, J., Wallace, S., 2012. Clogging in subsurface-flow treatment wetlands: measurement, modeling and management. Water Res. 46, 1625–1640. doi:10.1016/j.watres.2011.12.051.

Peszynska, M., Trykozko, A., Iltis, G., Schlueter, S., Wildenschild, D., 2016. Biofilm growth in porous media: experiments, computational modeling at the porescale, and upscaling. Adv. Water Resour. 95, 288–301. doi:10.1016/j.advwatres.2015.07.008.

Picioreanu, C., Blauert, F., Horn, H., Wagner, M., 2018. Determination of mechanical properties of biofilms by modelling the deformation measured using optical coherence tomography. Water Res. 145, 588–598. doi:10.1016/j.watres.2018.08.070.

Pintelon, T.R.R., Graf von der Schulenburg, D.A., Johns, M.L., 2009. Towards optimum permeability reduction in porous media using biofilm growth simulations. Biotechnol. Bioeng. 103, 767–779. doi:10.1002/bit.22303.

Pintelon, T.R.R., Picioreanu, C., van Loosdrecht, M.C.M., Johns, M.L., 2012. The effect of biofilm permeability on bio-clogging of porous media. Biotechnol. Bioeng. 109, 1031–1042. doi:10.1002/bit.24381.

Pousti, M., Zarabadi, M.P., Abbaszadeh Amirdehi, M., Paquet-Mercier, F., Greener, J., 2019. Microfluidic bioanalytical flow cells for biofilm studies: a review. Analyst 144, 68–86. doi:10.1039/C8AN01526K.

Qin, C.-.Z., Hassanizadeh, S.M., 2015. Pore-network modeling of solute transport and biofilm growth in porous media. Transp. Porous Media 110, 345–367. doi:10.1007/s11242-015-0546-1.

Radu, A.I., Vrouwenvelder, J.S., van Loosdrecht, M.C.M., Picioreanu, C., 2012. Effect of flow velocity, substrate concentration and hydraulic cleaning on biofouling of reverse osmosis feed channels. Chem. Eng. J. 188, 30–39. doi:10.1016/j.cej.2012.01.133.

Redman, J.A., Walker, S.L., Elimelech, M., 2004. Bacterial adhesion and transport in porous media: role of the secondary energy minimum. Environ. Sci. Technol. 38, 1777–1785. doi:10.1021/es034887l.

Rubol, S., Freixa, A., Carles-Brangarí, A., Fernàndez-Garcia, D., Romaní, A.M., Sanchez-Vila, X., 2014. Connecting bacterial colonization to physical and biochemical changes in a sand box infiltration experiment. J. Hydrol. 517, 317–327. doi:10.1016/j.jhydrol.2014.05.041.

Seymour, J.D., Gage, J.P., Codd, S.L., Gerlach, R., 2004. Anomalous fluid transport in porous media induced by biofilm growth. Phys. Rev. Lett. 93, 198103. doi:10.1103/PhysRevLett.93.198103.

Singh, R., Olson, M.S., 2012. Transverse chemotactic migration of bacteria from high to low permeability regions in a dual permeability microfluidic device. Environ. Sci. Technol. 46, 3188–3195. doi:10.1021/es203614y.

Stoodley, P., Debeer, D., Lewandowski, Z., 1994. Liquid flow in biofilm systems. Appl. Environ. Microbiol. 60, 2711–2716.

Subramanian, S., Huiszoon, R.C., Chu, S., Bentley, W.E., Ghodssi, R., 2020. Microsystems for biofilm characterization and sensing – a review. Biofilm 2, 100015. doi:10.1016/j.bioflm.2019.100015.

Tang, Y., Liu, H., 2017. Modeling multidimensional and multispecies biofilms in porous media. Biotechnol. Bioeng. 114, 1679–1687. doi:10.1002/bit.26292.

Taylor, S.W., Jaffé, P.R., 1990. Biofilm growth and the related changes in the physical properties of a porous medium: 3. dispersivity and model verification. Water Resour. Res. 26, 2171–2180. doi:10.1029/WR026i009p02171.

Thullner, M., Baveye, P., 2008. Computational pore network modeling of the influence of biofilm permeability on bioclogging in porous media. Biotechnol. Bioeng. 99, 1337–1351. doi:10.1002/bit.21708.

Valiei, A., Kumar, A., Mukherjee, P.P., Liu, Y., Thundat, T., 2012. A web of streamers: biofilm formation in a porous microfluidic device. Lab Chip 12, 5133. doi:10.1039/c2lc40815e.

Vandevivere, P., 1995. Bacterial clogging of porous media: a new modelling approach. Biofouling 8, 281–291. doi:10.1080/08927019509378281.

Walker, S.L., Redman, J.A., Elimelech, M., 2004. Role of cell surface lipopolysaccharides in Escherichia coli K12 adhesion and transport. Langmuir 20, 7736–7746. doi:10.1021/la049511f.

Wang, X., Liu, B., Pan, X., Gadd, G.M., 2019. Transport and retention of biogenic selenium nanoparticles in biofilm-coated quartz sand porous media and consequence for elemental mercury immobilization. Sci. Total Environ. 692, 1116–1124. doi:10.1016/j.scitotenv.2019.07.309.